Automated Robotic Measurement of 3-D Cell Morphologies

Jun Liu, Zhuoran Zhang, Xian Wang, Haijiao Liu, Qili Zhao, Chao Zhou, Min Tan, Huayan Pu, Shaorong Xie, and Yu Sun

Abstract—**Cell morphology plays an important role in maintaining normal cellular functions. Existing techniques for cell morphology measurement, such as confocal imaging and atomic force microscopy, have the limitations of photobleaching and incompatibility for integration with other cell manipulation instruments. This paper reports a robotic cell manipulation system that is capable of measuring changes of cell morphologies. This capability is enabled by several key techniques including cell recognition, determination of contact points on a cell, and two vision-based contact detection methods for measuring cell bottom and top surface positions. With the detected cell contour and height information, three-dimensional cell morphology is reconstructed. Experiments show that the cell morphology measurement technique has an overall success rate of 95.67%, an average measurement speed of 2.63 s/contact, and a measurement error of 4.65%. The cell morphology measurement results indicate that bladder cancer cells with higher metastatic potential exhibit lower cell heights than earlier-stage cancer cells because of more disorganized cytoskeleton networks. We also applied the robotic system to microinject the drug Cytochalasin D into cancer cells, and the drug effect on cell morphology changes was quantified.**

Index Terms—**Automation at micro-nano scales, biological cell manipulation.**

I. INTRODUCTION

THE synergy between robotics and cell biology has become increasingly strong over the past two decades. Robotic systems have been developed for patterning [1], grasping [2], and injecting single cells [3]. Here, this paper reports a robotic cell manipulation system that is, for the first time, capable of measuring 3D cell morphologies. Cell morphology plays a critical role in maintaining normal cellular functions including proliferation, migration, and interactions with the extracellular environment [4]. Abnormal morphological changes are related to diseases such as anemia, autoimmune diseases, and cancers [5]. Studying cell behaviors and investigating disease mechanisms such as cancer metastasis require three-dimensional (3D) cell morphology measurement and the monitoring of cell shape changes [6].

Presently, cell morphology measurements are made by atomic force microscopy (AFM) and confocal microscopy imaging. AFM has strong measurement capabilities, but cannot achieve cell manipulation tasks such as microinjection or pick-and-place of cells [7]. Furthermore, AFM is a stand-alone instrument; the integration of AFM with other robotic cell manipulation system is difficult. For cell morphology measurement, transferring cell samples after robotic cell manipulation onto an AFM stage can cause significant challenges in relocating target cells, and morphology changes can be missed during the time-consuming cell search process.

Confocal microscopy enables the reconstruction of 3D cell morphology by capturing fluorescent images at different Z depths. However, confocal imaging demands fluorescent staining or transgenetic labeling [8]. Additionally, during the long operation time (from several to tens of minutes) for collecting a high number of Z image stacks, laser exposure can lead to photobleaching that makes repeated cell morphology measurement infeasible.

For a robotic system to measure 3D cell morphology, determining heights along the Z direction with a high accuracy is a challenging task. Techniques of focus-defocus [9], force feedback [10], and electrical feedback [11] have been used for the determination of Z positions in existing robotic systems. Focusing-based methods dynamically align the focal plane with the target object by calculating focus measures. Autofocusing has poor Z position measurement accuracies, ranging from several to tens of micrometers. Moreover, the detection of the global maximum/minimum of focus measures can be trapped by local maxima/minima. Force sensors for measuring forces at micro and nanoNewton levels have been used for detecting the contact with cells. However, force sensors at this scale are fragile, and the integration with cell manipulation

J. Liu, Z. Zhang, X. Wang, H. Liu, Q. Zhao, and Y. Sun are with the Department of Mechanical and Industrial Engineering, University of Toronto, Toronto, ON M5S 3G8, Canada (e-mail: sun@mie.utoronto.ca).

C. Zhou and M. Tan are with the Institute of Automation, Chinese Academy of Sciences, Beijing 100190 China (e-mail: chao.zhou@ia.ac.cn; min.tan@ia.ac.cn).

H. Pu and S. Xie are with the authors are with the Department of Mechatronic Engineering, Shanghai University, Shanghai 200072, China (e-mail: phygood_2001@shu.edu.cn; srxie@shu.edu.cn).
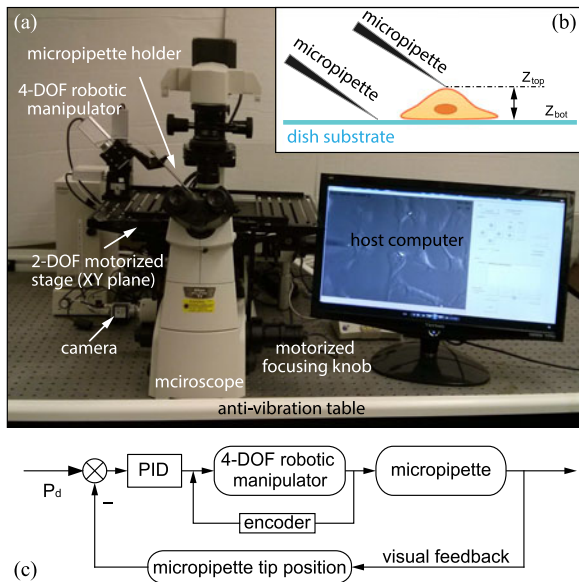
Fig. 1. (a) Robotic cell manipulation system for measuring cell morphology immediately after cell microinjection. (b) Cell height is measured by detecting the contact of micropipette tip on dish substrate and on cell membrane. (c) A 4-DOF robotic manipulator is controlled to position the micropipette tip via an image-based visual servo control system.

end-effectors (e.g., glass micropipettes) is notoriously difficult. Electrical impedance measurement was also proposed for the detection of cell-micropipette contact [12]. However, the technique requires the use of an electrode inside the micropipette and a detection circuit; the reliability and measurement accuracy can be influenced by variations of ion concentrations in cell culture medium.

This paper reports a robotic system that is capable of measuring 3D cell morphological changes via visually detecting the contact of the micropipette tip at multiple locations on the cell membrane. The system detects cell heights by integrating a new histogram-based thresholding method and two vision-based algorithms for detecting the contact of micropipette tip with dish substrate and cell top surface. System performance was calibrated against both confocal imaging and AFM measurement. The results demonstrate that the contact detection methods have an overall success rate of 95.67% and an average measurement speed of 2.63 s/contact. The system was also applied to microinjection of drug molecules (cytochalasin D) into two bladder cancer cell lines (T24 and RT4), and measured their morphological changes resulting from the effect of cytochalasin D on cytoskeleton networks.

II. System Overview

As shown in Fig. 1(a), the robotic cell manipulation system is built around an inverted microscope (Nikon Ti) that is equipped with motorized magnification control and motorized focusing. Mounted on the microscope is an XY motorized stage (ProScan, Prior Scientific Inc.) with a travel range of 75 mm and a resolution of 0.01 μm along both axes. Adherent cells cultured in 35-mm Petri dishes are placed on the motorized X-Y stage. A 4-DOF micromanipulator (MX7600L, Siskiyou Corp.)

is used to move a micropipette (outer diameter of 500 nm) to perform microinjection and to contact either the dish substrate or the cell surface for measuring cell morphologies. A camera (scA1300-32gm, Basler Inc.) is connected to the microscope to provide visual feedback. The micromanipulator and X-Y stage are cooperatively controlled for positioning the micropipette along XYZ and positioning cells in the XY plane, respectively. The control architecture for positioning the micropipette is summarized in Fig. 1(c). Microscopy visual feedback is used for providing position information to control the micromanipulator and X-Y stage, forming an image-based visual servo control system.

In operation, the system first locates the micropipette tip and positions it to the center of the field of view via an auto-locating technique we previously reported [13]. The 3D cell morphologies are reconstructed from the 2D cell shape detected in the X-Y plane and cell heights measured at multiple locations on the cell membrane. To measure the cell's bottom level and its heights, the robotic system moves the micropipette tip downwards to contact the cell culture dish substrate and contact the cell top surface, respectively [Fig. 1(b)]. Once the contacts are visually detected, the micropipette movement is stopped and the Z positions recorded from the robotic manipulator are taken by the system as the cell bottom (Z_{bot}) and top surface levels (Z_{top}). Key methods include the recognition of cells and empty areas on the culture dish substrate, contact detection on the dish substrate to determine the cell bottom surface level, and contact detection on cell membrane to determine cell heights.

III. Key Methods

A. Cell Recognition and Determination of Contact Points

1) Cell Recognition: The reconstruction of 3D cell morphology starts with the detection of 2D cell shapes in the X-Y plane (i.e., imaging plane). Under phase contrast imaging, the empty dish substrate is captured as the uniform background, whereas the cells reveal complex features from intracellular structures [see Fig. 2(a)]. Accordingly, the background pixels have the highest frequency in the image histogram [Fig. 2(b)]. In order to remove the background, the pixels between two neighboring local minimal frequencies [i.e., gray region in Fig. 2(b)] are set to zero. The foreground objects (i.e., cells) in the remaining pixel regions are set as the maximal pixel value to achieve the histogram-based thresholding.

After the thresholding step, small objects (cell debris) in the binarized image are eliminated by applying morphological transformations [Fig. 2(c)]. The external contour of each detected foreground object is drawn on the binarized image, and the internal holes in the cell region are filled by convex hull processing. When multiple cells cluster together, to segment the clustered neighboring cells, a distance transform algorithm is applied to detect the mass center of each cell. A perpendicular bisector line between the cell centers is used to segment the clustered cells. In the final step, the separated cell contours are fitted to ellipses, and the ellipse's long and short axes are determined [Fig. 2(d)].
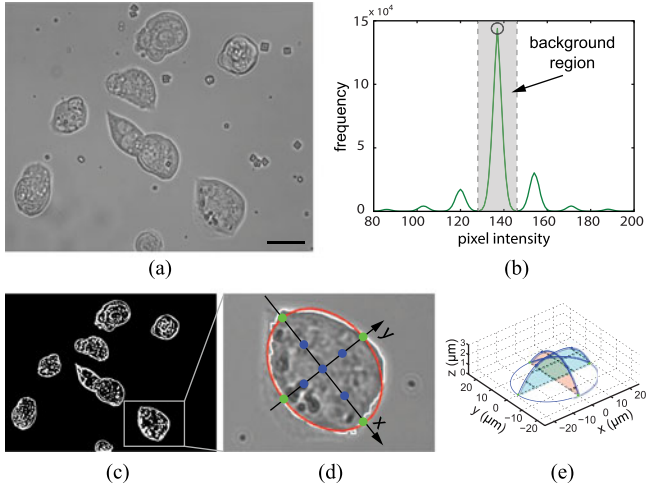
Fig. 2. Recognition of cells and contact points determination. (a) Original image shows multiple cells. (b) The image histogram shows the background region (i.e., gray area) has the highest frequency. (c) Cells are detected from the binarized image after morphological transformation. (d) Four intersections of the cell contour and the long/short axis (green dots), middle points of long/short axis and the center point of the ellipse (blue dots) are selected for fitting cubic splines. (e) An example of reconstructed cell morphology by fitting cubic splines.

2) Determination of Points for Height Measurement: After fitting an ellipse on the cell contour, the intersections between the cell contour and long/short axes of the ellipse (i.e., the green dots on cell edge in Fig. 2(d)) are selected for measuring cell morphology. In addition to these intersection points, two more points along either long or short axes are needed for fitting a cubic spline. Therefore, the two middle points on the long/short axes are also selected (i.e., blue dots on cell surface in Fig. 2(d)) for height measurement. Since the highest point on the cell is often located around the center position, the center point of the ellipse is also measured for achieving a more accurate spline fitting.

The four green dots in Fig. 2(d) are assumed on the same Z level, Z_{bot}, which is determined by contact detection on the culture dish substrate (Section III-B). The heights of the five blue dots in Fig. 2(d) are individually measured by contact detection on the cell membrane (Section III-C). Then, the 3D morphology is determined by cubic spline fitting [Fig. 2(e)].

B. Determination of Cell Bottom Surface Level

Because cultured cells strongly adhere to the culture dish substrate, the robotic system controls the micropipette tip and detects the contact with the cell culture dish substrate in order to determine the Z position of the cell bottom surface, Z_{bot}). When the micropipette tip moves downwards to contact the culture dish substrate, the tip movement in the world coordinate and its position changes in the image plane have a fixed geometrical relationship, as illustrated in Fig. 3(a). The distance between the micropipette tip and the objective is denoted by u, and the distance between the image plane and the objective is denoted by v. According to the principle of microscopy imaging, the micropipette tip position in the imaging plane (x-y) can be derived
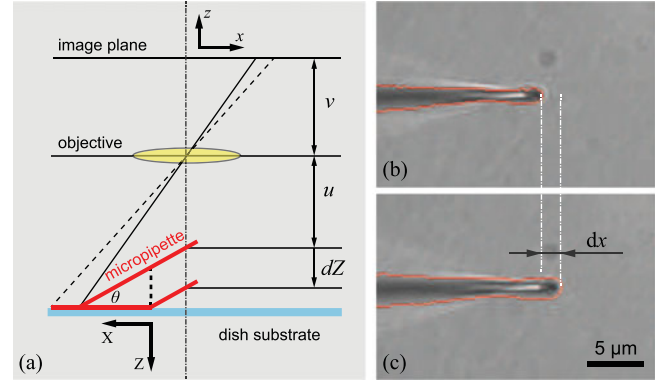

Fig. 3. Determination of cell bottom surface level. (a) The imaging diagram shows a fixed geometrical relationship between the micropipette movement in the world coordinate and its position changes in the image plane. (b), (c) Micropipette tip slides in the X-Y plane after contact is established.

from the tip location in the real world coordinate (*X-Y-Z*)

$$x = \frac{v \cdot X}{u + Z}. \tag{1}$$

After contacting the dish substrate, further lowering motion of the micropipette tip in the world coordinate (dZ) causes the tip to slide on the dish substrate, resulting in tip position changes in the imaging plane

$$dx = \frac{v}{u + Z} \cdot dX = \frac{v}{u + Z} \cdot \tan\frac{\theta}{2} \cdot \mathrm{d}Z \tag{2}$$

where θ is the tilting angle of the micropipette. Therefore, the tip-substrate contact is determined by detecting the tip sliding motion in the image frame.

To achieve a high accuracy for detecting the micropipette tip position, sub-pixel edge detection with Gaussian convolution is used. The blurry edge at the tip location can be modeled as a convolution of an ideal step function $\chi(x)$ with the Gaussian function $G(x)$,

$$I(x) = \chi(x) * G(x) = \int_{-\infty}^{\infty} \chi(x - u) G(u) \mathrm{d}u$$

$$= h + \frac{k}{\sqrt{2\pi}\sigma} \int_{-\infty}^{x} \exp\left[\frac{-(u - T)^2}{2\sigma^2}\right] \mathrm{d}u \tag{3}$$

where $I(x)$ is the gray scale value at location x; h and $h + k$ represent the pixel intensities on the darker and brighter side, respectively; T is the actual tip edge location; and σ is the standard deviation of Gaussian noise. The Gaussian convolution model well describes the real edge representation because it effectively models the defocusing or blurring phenomenon caused by the point-spread function of an optical system [14].

When the system detects an increment of the micropipette tip position (i.e., $T \uparrow$) as a result of the tip-substrate contact, the system stops lowering the micropipette, and the Z position feedback from the robotic manipulator is recorded as the culture dish substrate level (i.e., cell bottom position, Z_{bot}).
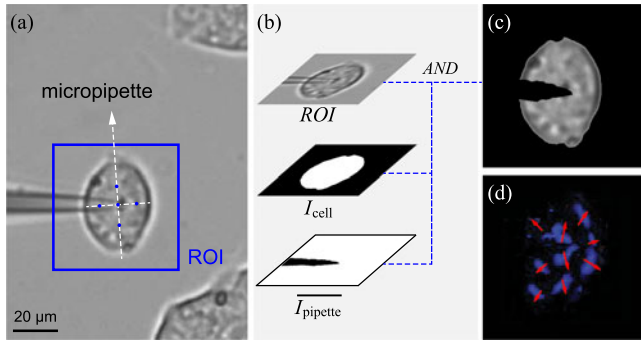
Fig. 4. Contact detection on cell membrane. (a) Original image shows region of interest (blue square) and the target contact points (blue dots). (b), (c) A new ROI is created by taking the conjunction of original ROI and the binarized cell mask with the micropipette tip excluded. (d) Motion history image shows enhanced cell deformation motion indicating the cell is being deformed. Red arrows represent motion gradients.

C. Determination of Cell Top Surface Levels

The detection of the Z positions of the five blue points labeled in Fig. 2(d) is achieved by controlling the micropipette tip to contact those points on the cell membrane. The system moves the micropipette tip to a location directly above the target contact point in the X-Y plane and then lowers the micropipette tip to approach the cell along the Z axis. When the tip contacts the cell membrane, the cell is deformed and a subtle deformation motion appears around the contact point. To detect this subtle motion, we have developed an algorithm based on motion history images (MHI) that can enhance the motion representations by accumulating the cell deformation over a short period of time.

In this process, a region of interest (ROI) is first extracted around the micropipette tip [Fig. 4(a)]. When the tip contacts the cell membrane, the motion image contains both cell deformation and micropipette's lowering motion. To remove the micropipette tip's lowering motion, the system further processes the image with a customized mask [Fig. 4(b)]. The mask is generated by calculating the conjunction of the original ROI and the binarized cell mask (I_{cell}) with the micropipette tip ($I_{pipette}$) excluded. The customized mask is

$$\text{ROI}' = \text{ROI} \cap I_{cell} \cap \overline{I_{pipette}}. \qquad (4)$$

The micropipette tip region is detected by using the histogram-based thresholding method when the micropipette is positioned above an empty region. When the micropipette contacts the cell membrane, the micropipette tip region is used to generate the customized mask. After removing the micropipette tip region [see Fig. 4(c)], cell deformation motion is calculated by frame subtraction and binarized with an adaptive thresholding method. The motion history image $H_\tau(x, y, t)$ is then constructed according to

$$
H_\tau(x, y, t) \\
= \begin{cases} \tau & \text{if } \Psi(x, y, t) = 1 \\ \max(0, \ H_\tau(x, y, t-1) - \gamma) & \text{otherwise} \end{cases} \qquad (5)
$$

where $\Psi(x, y, t)$ is the binary image representing the cell deformation motion; the time duration τ determines the temporal extent of the movement; and γ is the decay parameter. The binary image $\Psi(x, y, t)$ is calculated by taking the intensity differences between two successive images and then processed with the Otsu's thresholding method. The subtle cell deforming motion can be greatly enhanced by adding up the motion history information.

The motion gradients [Fig. 4(d)] are computed by a convolution of the Sobel filters to yield spatial derivatives, F_x and F_y. The orientation of the motion gradient at each moving component in MHI is

$$\Phi(x, y) = \arctan \frac{F_y(x, y)}{F_x(x, y)}. \qquad (6)$$

As the micropipette tip touches the cell membrane, deformation occurs around the contact point. Accordingly, the motion gradients in MHI converge to the contact point. In a successful contact detection, the motion gradients are radially distributed. Otherwise, the contact motion detection is considered to be a false positive case.

The sum of pixel values in MHI, $s(H_\tau)$, is calculated as a measure to detect the tip's contact on the cell membrane. If $s(H_\tau)$ is above a threshold value δ, the tip-cell contact is considered successfully detected. The system dynamically calculates the threshold δ by analyzing the changes of sum of pixel values of MHIs

$$\delta = \mu + a \cdot \sigma(s) \qquad (7)$$

where μ is the average value of the pixel sum of MHIs before micropipette tip-cell contact occurs; $\sigma(s)$ is the standard deviation; and a is a preset parameter which can be experimentally tuned, as discussed in more details in Section IV. By adding $a \cdot \sigma(s)$ to the mean value, the threshold δ is able to effectively reject those MHIs that do not contain cell deformation.

When the contact of the micropipette tip on cell membrane is successfully detected, the system stops lowering the micropipette and records the Z position from the encoder of the robotic manipulator which is regarded as Z_{top}. The cell height at the contact location is then $H = Z_{top} - Z_{bot}$. The system repeats this process until the heights of all the five blue points in Fig. 2(d) are measured. With the cell bottom surface level determined (four points on cell bottom surface) and the heights of five points on the cell membrane measured, the system constructs the 3D morphology of the cell by fitting two cubic splines along the long and short axes [Fig. 2(e)].

IV. RESULTS AND DISCUSSION

Two bladder cancer cell lines, RT4 and T24 cells were used in experiments for robotic manipulation and 3D morphology measurement. The cells were obtained from the American Type Culture Collection (ATCC, Manassas, VA) and cultured in McCoy's 5A modified medium with 10% FBS and 1% penicillin-streptomycin at 37 °C and 5% CO^2. Before use in experiments, T24 and RT4 cells were passaged and seeded at 200 cells/cm^2 in 35-mm Petri dishes for 24 h.

TABLE I
CONTACT DETECTION ON CELL MEMBRANE

Threshold value	$\mu + 3\sigma$	$\mu + 5\sigma$	$\mu + 7\sigma$	Average
Success rate (%)	93%	96%	98%	95.67%
Average time (sec)	2.43	2.65	2.84	2.63
Normalized error (%)	3.74%	4.35%	5.87%	4.65%

A. Success Rate and Speed of Contact Detection

Contact detection was repeated by using the micropipette tip to contact RT4 cells (5 points on each cell, 60 cells in total). A contact detected by the robotic system was considered successful when contact-induced cell deformation was confirmed independently by three skilled operators in the evaluation experiments. As discussed in Section III-C, the successful detection of tip-cell contact largely depends on the selection of the threshold value, $\delta = \mu + a \cdot \sigma$. Therefore, the experiments were separated into three groups by varying the factor a. The results summarized in Table I indicate that the average success rate for contact detection is (95.67±2.05%). The use of higher threshold values can reject more false positive detections that are caused by noise resulting from the defocusing shadow of the micropipette tip. Thus, a larger threshold value ($\mu+7\sigma$) produced a higher success rate (98% vs. 93%) than a smaller threshold value ($\mu+3\sigma$).

To evaluate the speed of contact detection on cell membrane, the average time shown in Table I represents the time taken for detecting a single point on the cell membrane. The results reveal that the selection of a relatively large threshold value results in a short time delay in detecting the micropipette tip-cell contact (2.84 s for $a = 7$ vs. 2.43 s for $a = 3$). Using a larger threshold value is more robust to noises and can produce a higher detection success rate; however, it sacrifices the sensitivity of detecting subtle cell deformation and costs a longer detection time.

B. Calibration With Confocal Microscopy and AFM

1) Confocal Calibration: To quantify the accuracy of robotic measurement, we measured the morphology of the same cell with confocal microscopy imaging. For confocal imaging, the membrane of the RT4 cells was labeled with a red fluorescent dye (CellMask™, ThermoFisher, Inc.). The membrane-labeled cell was imaged by a Nikon confocal microscope with a Z-stack resolution of 0.2 μm. After confocal imaging [Fig. 5(a)], the microscope was switched to the phase contrast imaging mode for performing cell morphology measurement with the robotic system. Fig. 5(b) shows the contact of the micropipette tip with cell membrane where the micropipette tip's Z position is the system detected contact position. The confocal measured height (H_1) was used as the benchmark value. Robotic measurement error (e) was calculated by taking the absolute difference between H_1 and the height determined by the robotic system, (H_2), $e=|H_1 - H_2|$. To take the height heterogeneity of cells into consideration, we further normalized the error with the confocal measured cell height (i.e., $e_{\text{norm}} = e/H_1$).

The results of the normalized detection errors are summarized in Table I and also shown in the box plot [Fig. 5(c)]. It can be
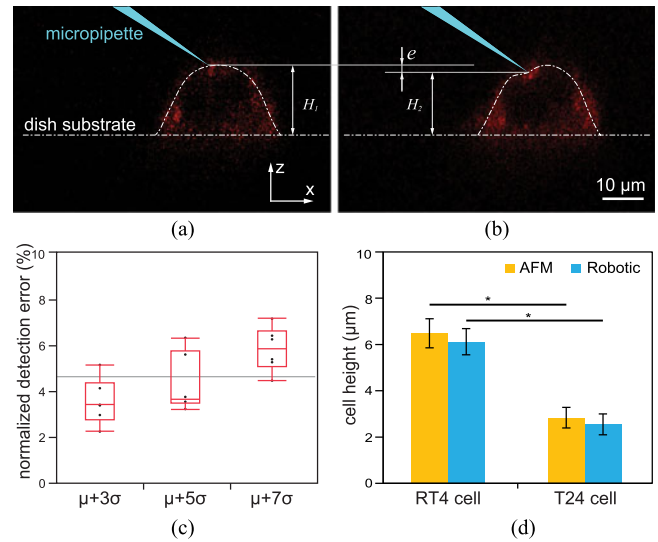

Fig. 5. Calibration with confocal microscopy and AFM. (a), (b) Side views of the confocal images show a cell before contact and during contact by a micropipette tip, respectively. (c) Larger threshold values led to higher normalized height measurement error. (d) Cell height measurements by AFM and the robotic system. Cancer cells of a higher metastasis grade (T24) reveal smaller cell heights than cancer cells of a lower metastasis grade (RT4). ∗ represents statistically significant difference.

seen that the selection of a large threshold value $\mu + 7\sigma$ resulted in the largest normalized error (5.87%). Although using a larger threshold value can achieve a higher success rate, it also causes a longer time delay for detecting cell deformation and leads to a larger measurement error. For results in the next two sections, a threshold value $\mu + 3\sigma$ was used for a higher measurement accuracy.

2) AFM Measurement: We next performed AFM (Bioscope, Bruker Corp.) measurement of cell heights on both T24 and RT4 cells and compared the results with those from robotic measurement. Instead of locating the same cells to perform AFM and robotic measurements, the cell population results were compared statistically. The results [Fig. 5(d)] show that there is no statistically significant difference ($p>0.05$) in measured cell heights between the AFM and robotic groups. However, a significant difference ($p<0.01$) between RT4 and T24 cells exists in both AFM and robotic measurements.

The later-stage cancer cells (T24) exhibit smaller cell heights (2.55 μm vs. 6.12 μm) than the early-stage cancer cells (RT4). To understand their height difference, we labeled the F-actin network with red phalloidin fluorescent dye (ThermoFisher Inc.) for both cell lines. F-actin is a major component of the cytoskeleton that supports the cell shape. Fluorescent imaging results revealed that T24 cells have a much lower density of F-actin than RT4 cells (65.8 vs 86.7 AU). F-actin network in T24 cells appears more disorganized and more fragmented than that in RT4 cells. These results are in agreement with previous studies [15] suggesting that morphological changes and "squish-like" cell behaviors are common characteristics of cancer cells in the cancer progression process.
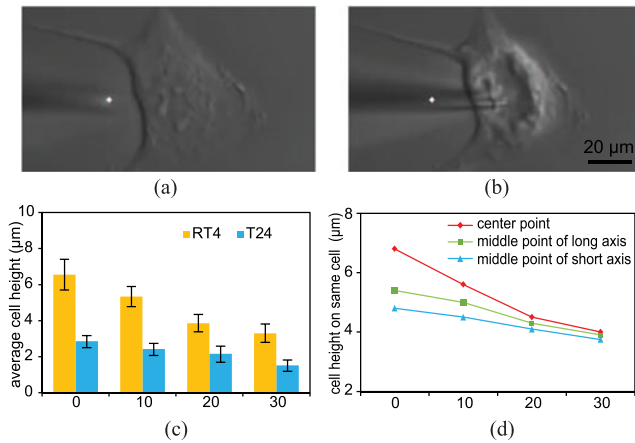
Fig. 6. Microinjection of Cytochalasin D into single cells, and measurement of cell morphology changes for assessing drug effect. (a) The micropipette tip approaches a target cell before microinjection. (b) The occurrence of a shock wave around the micropipette tip indicates a successful microinjection. (c) Microinjection of Cytochalasin D induces decreased cell heights. RT4 cells exhibit a greater decrease in cell height than T24 cells. (d) Height reduction at the cell center is larger than that at the middle points of the long/short axes.

C. Measurement of Cell Morphology Changes

The robotic system was next used for measuring cancer cells' morphology after microinjection with Cytochalasin D (1 μg/mL, ThermoFisher, Inc.). The robotic system controlled the position of the micropipette tip to penetrate the cell membrane, as we previously reported [16] and deposited Cytochalasin D into individual cells ($n = 60$ for each cell line). A successful microinjection is accompanied by a "shock wave" motion inside the cell around the microinjection location [Fig. 6(b)].

The robotic system then measured the drug-induced morphological changes immediately after microinjection and 10, 20, and 30 min post microinjection. As shown in Fig. 6(c), the average cell height significantly decreased for both T24 and RT4 after the drug delivery. The decrease in cell heights was caused by the disruption of intracellular actin networks, an effect from the microinjection of Cytochalasin D into the cells. Cytochalasin D is a member of mycotoxins that is known to disable the formation of actin microfilaments by activating the p53-dependent signaling pathways to prevent polymerization of actin monomers [17]. Cell heights were measured at multiple locations on each cell. As shown in Fig. 6(d), the height reduction at the center point is more significant than those at the four side locations (i.e., middle points of long/short axes labeled in Fig. 2(d)), indicating the cells were flattened by the destructive effect of Cytochalasin D on cytoskeleton networks.

D. Discussion

Robotic measurement based on contact detection produces a simplified representation of cell morphologies. Although both AFM and the robotic contact detection technique rely on measuring cell deformation for achieving 3D cell morphologies, the sensitivity in laser measurement of AFM cantilever deflection is inherently higher than the sensitivity of measuring

micropipette-induced cell deformation in robotic contact detection via optical microscopy imaging. Therefore, a larger cell deformation occurs before robotic measurement is capable of detecting the contact of the micropipette tip on the cell membrane. This lower sensitivity is reflected in the data summarized in Fig. 5(d) which shows that robotically measured cell heights are consistently lower than AFM measured results.

Similar to AFM and confocal measurements, a trade-off between measurement speed and measurement accuracy also exists in robotic cell morphology measurement. The five-point contact approach presented in this paper, calibrated by AFM and confocal measurements, achieved an average error of 4.65% in cell height measurement (see Table I). However, for more accurate 3D morphology mapping, contacting more points on the cell membrane is required, which would also entail a longer measurement time.

V. CONCLUSION

This paper reported an automated robotic system that is capable of measuring 3D cell morphologies. This capability was enabled by several key techniques, including cell recognition, determination of contact points on a cell, contact detection on the cell culture dish substrate and on cell membrane. To achieve a high measurement accuracy, a sub-pixel edge detection algorithm was used to detect the micropipette tip's sliding motion on the cell culture dish substrate for the determination of cell bottom surface level. An MHI-based motion detection algorithm was developed to detect the subtle cell deformation during micropipette-cell membrane contact for measuring the Z positions of multiple points on the cell. Calibration by using AFM and confocal microscopy confirmed that the robotic system is capable of measuring 3D cell morphologies with a high success rate and a high accuracy. The robotic system also delivered a drug molecule, Cytochalasin D into cancer cells, and the drug's effect on disrupting intracellular cytoskeleton networks was assessed by quantifying cell morphology changes.

REFERENCES

[1] Z. Lu, C. Moraes, G. Ye, C. A. Simmons, and Y. Sun, "Single cell deposition and patterning with a robotic system," *PloS One*, vol. 5, no. 10, 2010, Art. no. e13542.

[2] X. Liu, K. Kim, Y. Zhang, and Y. Sun, "Nanonewton force sensing and control in microrobotic cell manipulation," *Int. J. Robot. Res.*, vol. 28, no. 8, pp. 1065–1076, 2009.

[3] H. Ladjal, J.-L. Hanus, and A. Ferreira, "Micro-to-nano biomechanical modeling for assisted biological cell injection," *IEEE Trans. Biomed. Eng.*, vol. 60, no. 9, pp. 2461–71, Sep. 2013.

[4] T. Lecuit and P.-F. Lenne, "Cell surface mechanics and the control of cell shape, tissue patterns and morphogenesis," *Nature Rev. Mol. Cell Biol.*, vol. 8, no. 8, pp. 633–644, 2007.

[5] Y. Wang *et al.*, "Morphology, in vivo distribution and antitumor activity of bexarotene nanocrystals in lung cancer," *Drug Dev. Ind. Pharm.*, pp. 1–10, 2016.

[6] J. Liu, J. Wen, Z. Zhang, H. Liu, and Y. Sun, "Voyage inside the cell: Microsystems and nanoengineering for intracellular measurement and manipulation," *Microsyst. Nanoeng.*, vol. 1, 2015, Art. no. 15020.

[7] D. J. Müller and Y. F. Dufrêne, "Atomic force microscopy: A nanoscopic window on the cell surface," *Trends Cell Biol.*, vol. 21, no. 8, pp. 461–469, 2011.

[8] R. H. Webb, "Confocal optical microscopy," *Rep. Prog. Phys.*, vol. 59, no. 3, 1996, Art. no. 427.

[9] B. Tamadazte, N. L.-F. Piat, and S. Dembélé, "Robotic micromanipulation and microassembly using monoview and multiscale visual servoing," *IEEE/ASME Trans. Mech.*, vol. 16, no. 2, pp. 277–287, Apr. 2011.

[10] Y. Xie, D. Sun, H. Y. G. Tse, C. Liu, and S. H. Cheng, "Force sensing and manipulation strategy in robot-assisted microinjection on zebrafish embryos," *IEEE/ASME Trans. Mech.*, vol. 16, no. 6, pp. 1002–1010, Dec. 2011.

[11] K. Sakaki, N. Dechev, R. D. Burke, and E. J. Park, "Development of an autonomous biological cell manipulator with single-cell electroporation and visual servoing capabilities," *IEEE Trans. Biomed. Eng.*, vol. 56, no. 8, pp. 2064–2074, Aug. 2009.

[12] P. Kallio, T. Ritala, M. Lukkari, and S. Kuikka, "Injection guidance system for cellular microinjections," *Int. J. Robot. Res.*, vol. 26, no. 11–12, pp. 1303–1313, 2007.

[13] J. Liu *et al.*, "Locating end-effector tips in robotic micromanipulation," *IEEE Trans. Robot.*, vol. 30, no. 1, pp. 125–130, Feb. 2014.

[14] W. Zhang and F. Bergholm, "Multi-Scale blur estimation and edge type classification for scene analysis," *Int. J. Comput. Vis.*, vol. 24, no. 3, pp. 219–250, 1997.

[15] B. D. Craene and G. Berx, "Regulatory networks defining EMT during cancer initiation and progression," *Nature Rev. Cancer*, vol. 13, no. 2, pp. 97–110, 2013.

[16] J. Liu *et al.*, "Robotic adherent cell injection for characterizing cell-cell communication," *IEEE Trans. Biomed. Eng.*, vol. 62, no. 1, pp. 119–125, Jan. 2015.

[17] J. A. May, H. Ratan, J. R. Glenn, W. Losche, P. Spangenberg, and S. Heptinstall, "GPIIB-IIIA antagonists cause rapid disaggregation of platelets pre-treated with cytochalasin D. Evidence that the stability of platelet aggregates depends on normal cytoskeletal assembly," *Platelets*, vol. 9, no. 3/4, pp. 227–232, 1998.